Applied Physics Letters

RESEARCH ARTICLE | APRIL 08 2025

Deep sub-wavelength broadband metasurface with micro-perforated panels and extended-neck Helmholtz resonators

Jiayu Wang; Gareth J. Bennett

Appl. Phys. Lett. 126, 141703 (2025)
https://doi.org/10.1063/5.0258251

Deep sub-wavelength broadband metasurface with micro-perforated panels and extended-neck Helmholtz resonators

Cite as: Appl. Phys. Lett. **126**, 141703 (2025); doi: 10.1063/5.0258251
Submitted: 15 January 2025 · Accepted: 22 March 2025 ·
Published Online: 8 April 2025

Jiayu Wang[a] and Gareth J. Bennett[a]

AFFILIATIONS

Department of Mechanical, Manufacturing and Biomedical Engineering, Trinity College Dublin, The University of Dublin, D02 PN40 Dublin, Ireland

[a]Authors to whom correspondence should be addressed: wangj12@tcd.ie and gareth.bennett@tcd.ie

ABSTRACT

This study develops, fabricates, and characterizes a deep sub-wavelength broadband acoustic metasurface for noise absorption. The metasurface is composed of micro-perforated panels coupled with extended-neck Helmholtz resonators, forming a unit absorber referred to as Helmholtz resonator absorber (MHA). Experimental results demonstrate that a 48 mm deep MHA achieves near-perfect sound absorption (>97%) at 150 Hz. This performance is realized with a sub-wavelength thickness of only 1/48 of the operating wavelength and a volume-normalized wavelength ratio of 1/54. Additionally, the MHA exhibits a half-absorption bandwidth of 48 Hz. To broaden the sound absorption bandwidth while keeping the total area constant and to further reduce the total thickness, a configuration integrating three Compact MHA (CMHA) units is proposed. Experimental results demonstrate that the CMHA achieves an average sound absorption coefficient (SAC) exceeding 0.74 in the 300–500 Hz range with an overall thickness of only 27.5 mm and an SAC > 0.88 in the 543–945 Hz range with a reduced thickness of 26.2 mm. Experimental results compare well with theoretical and numerical predictions, highlighting the potential of the proposed design for practical noise control applications.

Addressing low-frequency noise remains a significant challenge in acoustic engineering. Theoretical and practical constraints stem from the physical requirement that effective sound absorption relies on material depths of at least one-quarter of a wavelength ($\lambda/4$), necessitating considerable material thicknesses for low-frequency attenuation.[1–9] This limitation not only increases material size and weight but also restricts the application of such absorbers in compact or weight-sensitive environments, such as aerospace, land-based transportation, or urban infrastructure. Developing low-frequency broadband sound absorbers at a deep sub-wavelength scale, where the physical depth of the absorber is significantly shorter than the wavelength of the targeted noise, remains one of the foremost challenges in sound control technologies.

To address this challenge, various innovative approaches have been developed to enhance low-frequency broadband absorption by combining or modifying conventional acoustic structures. These approaches include multi-chamber or multi-layer micro-perforated panel absorbers,[10–15] wavy or inhomogeneous micro-perforated panel absorbers,[16–20] micro-perforated panel absorbers with coiled chambers[21–23] and hybrid systems that integrate micro-perforated panel absorbers with Helmholtz resonators,[2–4,7,24] decorated membranes,[1,25–30] or porous materials.[7,31–33] While these methods demonstrate promising low-frequency absorption performance, they are often accompanied by limitations in structural thickness, tunability, or manufacturing complexity. The present study introduces an acoustic metasurface that combines a micro-perforated panel with an extended-neck Helmholtz resonator. This design is tailored to achieve efficient noise absorption at frequencies below 200 Hz on a deep sub-wavelength scale, while also providing broadband absorption across the 200–1000 Hz range. The proposed solution not only offers effective acoustic performance but also serves as a structurally robust and environmentally clean acoustic liner, making it a promising candidate for practical applications.

Figures 1(a) and 1(b) illustrate our design aimed at minimizing the thickness of the acoustic absorber while optimizing space utilization: a perforated panel with holes of diameter, d, and porosity, ϕ, backed with an air cavity (AC1) and coupled with an embedded extended-neck Helmholtz resonator (HR) absorber, hereafter referred

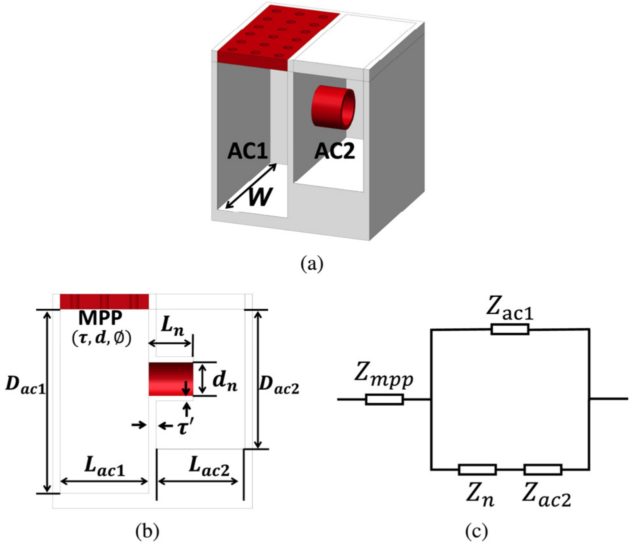

FIG. 1. MHA design. (a) Three-dimensional schematic. (b) Two-dimensional cross section. (c) Equivalent circuit model.

to as MHA. The resonator's neck, of internal diameter d_n and length L_n, is designed to extend into an adjoining cavity (AC2). The micro-perforated top panel has a thickness of τ and dimensions of L_{ac1} and W. Similarly, the non-perforated top panel, also with a thickness of τ, has dimensions of L_{ac2} and W. The depth of AC1 is denoted by D_{ac1}. The "depth" of the HR cavity (AC2), denoted by D_{ac2}, is defined relative to the incident plane wave. The axis of the extended neck is positioned at the mid-point of D_{ac2}, provided that $D_{ac1} \geq D_{ac2}$. If this condition cannot be met, the axis of the extended neck is positioned at half of D_{ac1}. The wall thickness of the Helmholtz resonator's neck is τ' and is set to be equal to the thickness of the panel separating the two cavities. The total thickness (depth), H, of the MHA is calculated by adding τ to the larger of D_{ac1} or D_{ac2}.

When a plane acoustic wave is incident normal to the micro-perforated panel (MPP), the specific acoustic impedance of the MPP, denoted as z_{mpp} and defined in the following equation, can be treated as the ratio of the sound pressure difference (Δp) across the MPP to the product of the average particle velocity ($\bar{u}$) over the perforation area and the MPP porosity (ϕ):

$$z_{\mathrm{mpp}} = \frac{\Delta p}{\phi \bar{u}}. \tag{1}$$

According to Maa,[34] the specific acoustic impedance z_{mpp} for an MPP with circular perforations can be calculated using the following equation, where the dependence of the variables on angular frequency ω in this equation and in most others is omitted for brevity,

$$z_{\mathrm{mpp}} = \frac{\mathrm{i}\omega\tau}{c_0\phi}\left[1 - \frac{2}{\mathrm{Sh}\sqrt{-\mathrm{i}}}\frac{J_1(\mathrm{Sh}\sqrt{-\mathrm{i}})}{J_0(\mathrm{Sh}\sqrt{-\mathrm{i}})}\right]^{-1} + \frac{2\alpha_s R_S}{\rho_0 c_0 \phi} + \mathrm{i}\delta_s\omega\frac{d}{2c_0\phi}. \tag{2}$$

The $\exp(\mathrm{i}\omega t)$ convention is used in this work. Here, i denotes the imaginary unit, ρ_0 is indicative of the air density, and c_0 represents the speed of sound within air. The angular frequency, ω, is formulated as $\omega = 2\pi f$, with f signifying the frequency, measured in Hertz. J_m represents the mth order Bessel function. $\mathrm{Sh} = d\sqrt{\omega\rho_0/(4\mu)}$ is the shear number, and μ symbolizes the dynamic viscosity of air. The corresponding air properties used can be found in Table I. The current study does not consider the nonlinear effects of the MPP.

In Eq. (2), $\frac{2\alpha_s R_S}{\rho_0 c_0 \phi}$ represents the resistive end-correction, where R_S is the surface resistance on one side of the plate, calculated by $R_S = 0.5\sqrt{2\omega\rho_0\mu}$. The term $\mathrm{i}\delta_s\omega\frac{d}{2c_0\phi}$ represents the reactive end-correction. For the calculation of the non-dimensional resistive end-correction coefficient α_s and the non-dimensional reactive end-correction coefficient δ_s for perforations with sharp edges, Temiz *et al.*[35] proposed a practical expression, as shown in the following equation, valid when $1 < \mathrm{Sh} < 35$, and nonlinear effects are not present in the MPP,

$$\begin{aligned} \alpha_s &= 5.08\mathrm{Sh}^{-1.45} + 1.70 - 0.002/(\tau/d), \\ \delta_s &= 0.97\exp(-0.20\mathrm{Sh}) + 1.54 - 0.003/(\tau/d). \end{aligned} \tag{3}$$

The Helmholtz resonator, as illustrated in Fig. 1, studied in this paper is characterized by a neck extending into the cavity. The specific acoustic impedance of the Helmholtz resonator's neck can be calculated using the following equation:[4]

$$z_{\mathrm{n}} = \frac{1}{\phi_n}\left(z_N + 2\sqrt{2\omega\rho_0\mu} + \mathrm{i}\omega\rho_0\delta\right), \tag{4}$$

where $\phi_n = A_n/A_{\mathrm{hr}}$ represents the ratio of the inner cross-sectional area ($A_n = \pi d_n^2/4$) of the Helmholtz resonator neck to the contact area ($A_{hr} = W \times \min[D_{ac1}, D_{ac2}]$) between the two cavities.

In Eq. (4), the term

$$z_N = -\rho_0 c_0 \frac{2\mathrm{i}\sin\left(\frac{k_{c,n}L_n}{2}\right)}{\sqrt{(\gamma - (\gamma-1)Y_h)Y_v}} \tag{5}$$

symbolizes the specific acoustic impedance of the HR neck. Due to the considerable length of the Helmholtz neck, it is necessary to account for both viscous and thermal losses. γ is the specific heat ratio of air.

The complex wavenumber, $k_{c,n}$, in the cylindrical HR neck, which accounts for both viscous and thermal losses, can be expressed as follows:

$$k_{c,n} = k_0\sqrt{\left(\frac{\gamma - (\gamma-1)Y_{h,n}}{Y_{v,n}}\right)}. \tag{6}$$

The viscous function of the cylindrical HR neck, $Y_{v,n}$, and the thermal function of the cylindrical HR neck, $Y_{h,n}$, are shown in the following equation:

TABLE I. Air properties involved in the current study.

Air density	ρ_0	$1.204\ \mathrm{kg/m^3}$
Speed of sound	c_0	$343\ \mathrm{m/s}$
Dynamic viscosity	μ	$1.81 \times 10^{-5}\ \mathrm{kg/(ms)}$
Ratio of specific heats	γ	1.4
Specific heat capacity	C_p	$1005\ \mathrm{J/(kg\cdot K)}$
Thermal conductivity	K	$0.0257\ \mathrm{W/(m\cdot K)}$

$$Y_{v,n} = -\frac{J_2(k_v d_n/2)}{J_0(k_v d_n/2)},\quad Y_{h,n} = -\frac{J_2(k_h d_n/2)}{J_0(k_h d_n/2)}, \tag{7}$$

where the acoustic wave number k_0, viscous wave number k_v, and the thermal wave number k_h are defined as

$$k_0 = \frac{\omega}{c},\quad k_v^2 = -\mathrm{i}\omega\frac{\rho_0}{\mu},\quad k_h^2 = -\mathrm{i}\omega\frac{\rho_0 C_p}{K}, \tag{8}$$

where C_p is the specific heat at constant pressure, and K is the fluid thermal conductivity.

In Eq. (4), the term $2\sqrt{2\omega\rho_0\mu}$ represents the end-correction for the acoustic resistance, accounting for frictional losses attributed to the internal boundaries of the HR neck. Similarly, the term $\mathrm{i}\omega\rho_0\delta$ represents the end-correction for the acoustic reactance due to acoustic wave radiation. The total length end-correction in the neck, $\delta = \delta_1 + \delta_2$, is the sum of the length corrections at both ends of the neck. The transition from the MPPA cavity (AC1) to the neck approximates a flanged pipe termination; thus, the corresponding length end-correction δ_1 is given by[36]

$$\delta_1 = \delta_\infty + \frac{d_n/2}{b}(\delta_0 - \delta_\infty) + 0.057\frac{d_n/2}{b}\left[1 - \left(\frac{d_n/2}{b}\right)^5\right] d_n/2, \tag{9}$$

where $\delta_\infty = 0.8216(d_n/2)$ is the length end-correction of an infinitely flanged pipe and $\delta_0 = 0.6133(d_n/2)$ is the length end-correction of an ideal unflanged pipe. The parameter b is an "effective" value for a rectangular flange; In this study, b is calculated as $b = \sqrt{WD_{ac1}/\pi}$. The transition from the neck to the HR cavity (AC2) approximates an unflanged pipe termination with a thin wall thickness, τ', so the length end-correction, δ_2, should be[36]

$$\delta_2 = \delta_\infty + \frac{d_n/2}{d_n/2+\tau'}(\delta_0 - \delta_\infty) + 0.057\frac{d_n/2}{d_n/2+\tau'}\left[1 - \left(\frac{d_n/2}{d_n/2+\tau'}\right)^5\right]\frac{d_n}{2}. \tag{10}$$

Regarding the impedance of the air cavities, as $\lambda \gg H$, uniform pressure can be assumed within the air cavities and so the specific acoustic impedances of AC1 and AC2 can be defined as

$$z_{ac1} = -\mathrm{i}\frac{\rho_{ac}c_{ac}^2}{\omega V_{ac1}}A_{ac1},\quad A_{ac1} = L_{ac1}W,\qquad z_{ac2} = -\mathrm{i}\frac{\rho_{ac}c_{ac}^2}{\omega V_{ac1}}A_{ac2},\quad A_{ac2} = D_{ac2}W, \tag{11}$$

where $V_{ac1} = L_{ac1}\times W \times D_{ac1}$ is the volume of AC1, $V_{ac2} = L_{ac2}\times W\times D_{ac2} - \pi(d_n/2+\tau')^2\times(L_n-\tau')$ is the volume of AC2 minus the volume occupied by the HR neck. In interest of completeness, thermal and viscous losses in the cavities are also modeled,

$$\rho_{ac} = \frac{\rho_0}{Y_{v,ac}},\quad c_{ac} = \frac{\omega}{k_{c,ac}}, \tag{12}$$

where the wavenumber, $k_{c,ac}$, in the rectangular air cavity, which accounts for both viscous and thermal losses, can be expressed as follows:

$$k_{c,ac} = k_0\sqrt{\left(\frac{\gamma-(\gamma-1)Y_{h,ac}}{Y_{v,ac}}\right)}. \tag{13}$$

The viscous function, $Y_{v,ac}$, and the thermal function, $Y_{h,ac}$, of the rectangular air cavity with cross-sectional dimensions A and B are shown in the following equation:[37]

$$Y_{v,ac} = k_v^2\sum_{m=0}^{\infty}\left[\frac{1-\dfrac{\tan(\alpha_{m,v}A/2)}{\alpha_{m,v}A/2}}{(\alpha_{m,v}m')^2} + \frac{1-\dfrac{\tan(\beta_{m,v}B/2)}{\beta_{m,v}B/2}}{(\beta_{m,v}m')^2}\right],\quad Y_{h,ac} = k_h^2\sum_{m=0}^{\infty}\left[\frac{1-\dfrac{\tan(\alpha_{m,h}A/2)}{\alpha_{m,h}A/2}}{(\alpha_{m,h}m')^2} + \frac{1-\dfrac{\tan(\beta_{m,h}B/2)}{\beta_{m,h}B/2}}{(\beta_{m,h}m')^2}\right], \tag{14}$$

where $m' = (m+1/2)\pi$ and

$$\alpha_{m,v} = \sqrt{k_v^2 - \left(\frac{2m'}{A}\right)^2},\quad \beta_{m,v} = \sqrt{k_v^2 - \left(\frac{2m'}{B}\right)^2},\quad \alpha_{m,h} = \sqrt{k_h^2 - \left(\frac{2m'}{A}\right)^2},\quad \beta_{m,h} = \sqrt{k_h^2 - \left(\frac{2m'}{B}\right)^2}. \tag{15}$$

For AC1, let $A = L_{ac1}$ and $B = W$. For AC2, let $A = D_{ac2}$ and $B = W$.

The total specific impedance of the MHA, as derived from the equivalent circuit model, depicted in Fig. 1(c), can be calculated using the following equation:

$$z_{\text{mha}} = \left(Z_{\text{mpp}} + \frac{1}{1/Z_{\text{ac1}} + 1/(Z_{\text{n}} + Z_{\text{ac2}})}\right)\times A_{\text{surface}}. \tag{16}$$

It should be noted that each specific acoustic impedance in the circuit must be normalized by the cross-sectional surface area of the acoustic element.[28,38] Consequently, the acoustic impedances are calculated as follows: $Z_{\text{mpp}} = z_{\text{mpp}}/A_{\text{mpp}}$, $Z_{\text{ac1}} = z_{\text{ac1}}/A_{\text{ac1}}$, $Z_{\text{n}} = z_{\text{n}}/A_{\text{n}}$, and $Z_{\text{ac2}} = z_{\text{ac2}}/A_{\text{ac2}}$. As illustrated in Figs. 1(a) and 1(b), the surface area of the elementary cell is expressed as $A_{\text{surface}} = (L_{ac1} + L_{ac2} + \tau')\times(W)$.

In this study, a single MHA experimental sample, designated MHA-I, was optimized for the single target frequency of 150 Hz and subsequently fabricated. The MHA-I sample was 3D-printed using a Masked Stereolithography Apparatus (MSLA), as shown in Fig. 2(a). The maximum depth of the sub-chamber air cavity is 45 mm, and the total thickness, including the facesheet thickness of τ, is 48 mm. The optimization process and optimized geometric parameters of the MHA-I sample are provided in the supplementary material. The sound absorption coefficient and acoustic impedance of the MHA-I experimental sample were measured using the two-microphone tube in accordance with the ISO 10534-2:2023 standard.[39] Details of the experimental setup are provided in the supplementary material. To further validate the theoretical model, a three-dimensional finite element model was developed using the thermo-viscous acoustic module in COMSOL Multiphysics 6.0, as illustrated in Fig. 3(a). As for this case, the MHA-I model exhibits symmetry in the xy-plane, to optimize computational efficiency, only one half of the MHA-I geometry was simulated, with symmetry boundary conditions applied to the corresponding plane. The thermo-viscous acoustic module was

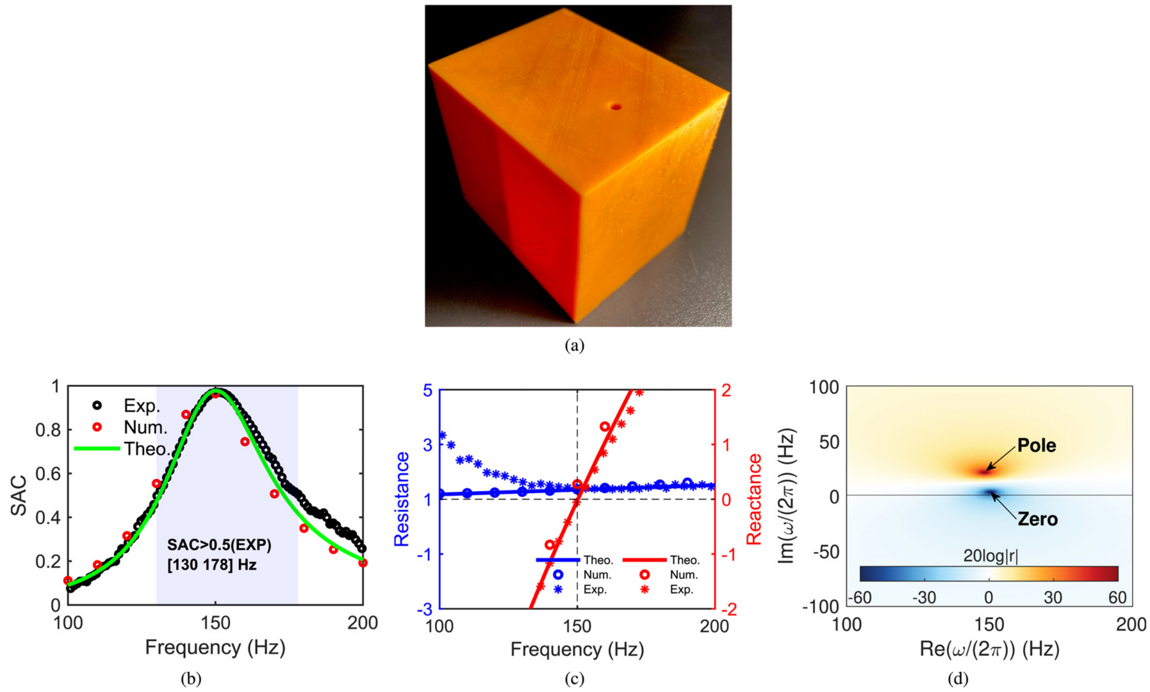

FIG. 2. (a) Photograph of MHA-I with a thickness of 48 mm. (b) Theoretical, numerical, and experimental SAC. (c) Theoretical, numerical, and experimental acoustic resistance and reactance. (d) Complex frequency plane representation of $20\log|R|$.

implemented to model all air domains, including the Helmholtz extended neck, aperture, air cavities (AC1 and AC2), and the upstream region of the tube. A normally incident plane wave pressure field was generated upstream of the test section. All structural walls of the MHA are represented by sound hard boundaries. Figure 3(b) illustrates the details of the meshed domains. Details of the mesh generation process can be found in the supplementary material.

Figure 2(b) illustrates the theoretical, numerical, and experimental sound absorption coefficients (SAC) of MHA-I. The theoretical and numerical results show excellent agreement with the experimental data. This consistency validates the accuracy of both the theoretical model and the finite element model. The fabricated MHA-I sample demonstrates near-perfect sound absorption ($\mathrm{SAC} > 0.97$) at its resonance frequency, $f_r = 150$ Hz, with a thickness of only 48 mm (less than two inches), which corresponds to approximately 1/48 of the operating wavelength. To characterize the sub-wavelength nature of the resonator while explicitly considering its total volume, we define a volume-normalized wavelength ratio as

$$\Gamma = \frac{V^{1/3}}{\lambda}, \tag{17}$$

where V represents the total volume of the resonator. This parameter reflects the overall volumetric constraint, rather than focusing solely on the resonator's thickness. A smaller Γ indicates a more compact sub-wavelength design, demonstrating the capability of achieving low-frequency resonance within a minimized resonator volume. The total volume of MHA-I is $V = 40 \times 40 \times 48\,\mathrm{mm}^3$, and thus the volume-normalized wavelength ratio is $\Gamma = 1/54$.

Additionally, the sample exhibits a sound absorption coefficient exceeding 0.5 over the frequency range of 130–178 Hz, yielding a frequency interval $\triangle f = 178–130 = 48$ Hz. This corresponds to an absorption bandwidth of 32% ($\triangle f/f_r$), indicating excellent low-frequency sound absorption performance at sub-wavelength scales. The acoustic absorption capabilities of the MHA-I can also be explained by its acoustic reactance and resistance, as illustrated in Fig. 2(c). An ideal impedance match is achieved when the normalized acoustic reactance is zero, and the acoustic resistance equals one. As shown in Fig. 2(b), at $f_r = 150$ Hz, the experimental acoustic reactance approaches zero, and the experimental acoustic resistance nears one, consistent with the experimental absorption curve at this frequency, where the experimental SAC is close to unity.

To effectively analyze absorption characteristics and illustrate the relationship between energy leakage and energy loss, along with their influencing factors, we employ the concept of the complex frequency plane.[40–42] By introducing an imaginary component, $\mathrm{Im}(\omega/(2\pi))$, to the frequency and substituting the complex frequency into the theoretical modeling, the reflection-related coefficient, $20\log(|r|)$, can be represented within the complex frequency plane to reveal its physical properties. In this context, the minimum and maximum values of $20\log(|r|)$ within the complex frequency domain are referred to as "zero" and "pole," respectively. It is crucial to note that the signs of the imaginary parts of poles and zeros depend on the time convention, specifically $\exp(i\omega t)$ in this study. In a lossless system, the zeros and poles of the reflection coefficient are symmetrically distributed about the real frequency axis. In such a system, energy leakage cannot be compensated by energy loss, leading to poor absorption performance. In the current work, as shown in Fig. 2(d), a zero of the MHA-I is

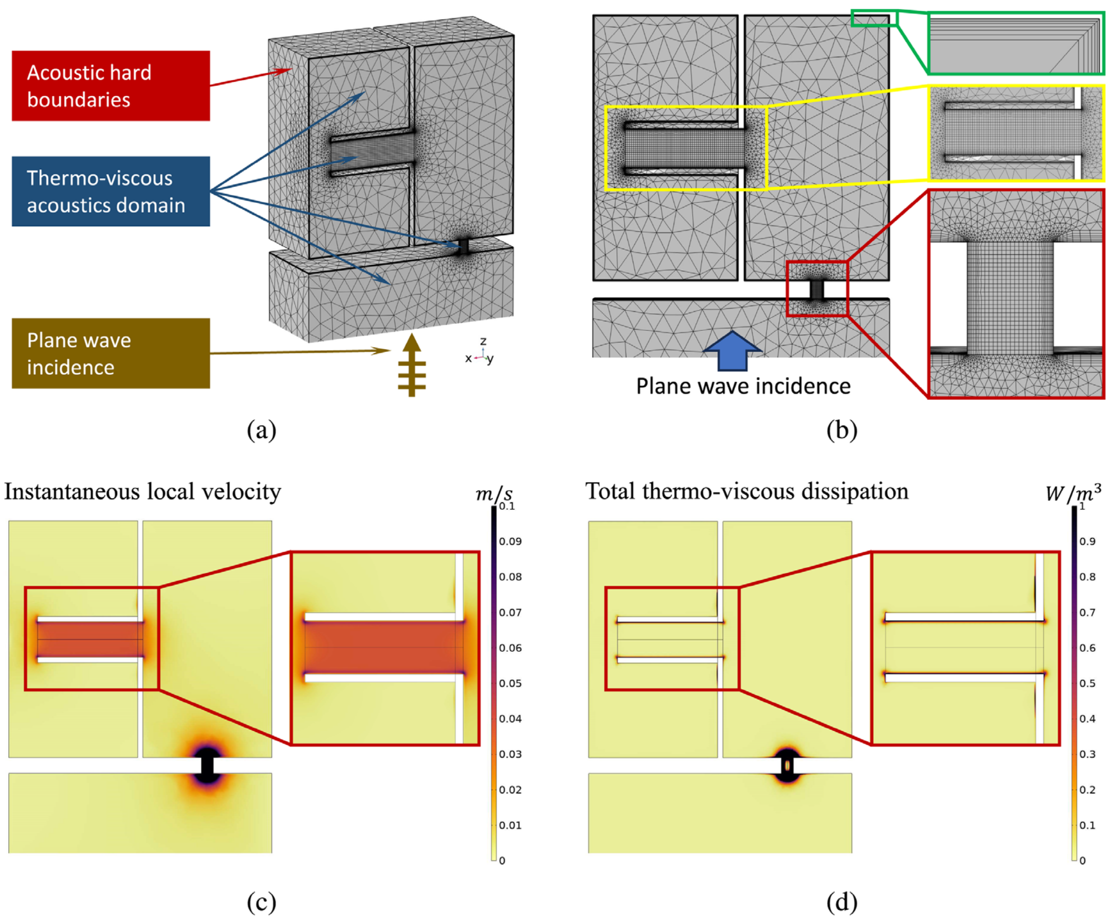

FIG. 3. (a) Three-dimensional finite element model of the MHA-I. (b) Details of the mesh configuration. (c) and (d) Simulated instantaneous local velocity field and total thermo-viscous dissipation field at $f_r = 150$ Hz.

located near the real frequency axis at $f_r = 150$ Hz, where the system's energy loss nearly balances its energy leakage. This balance satisfies the criteria for critical coupling, resulting in near-perfect absorption at this frequency.

To further investigate the perfect sound absorption mechanism of the MHA-I at the resonance frequency $f_r = 150$ Hz, Figs. 3(c) and 3(d) present the instantaneous velocity field and the total thermo-viscous dissipation rate distribution in the symmetry plane of the MHA-I model. At the resonance frequency, as shown in Fig. 3(c), the maximum instantaneous velocity is observed within the perforation, followed by the walls of the Helmholtz neck. Significant velocity is also detected near the entrance and exit edges of the perforation and the Helmholtz neck, which can be attributed to geometric discontinuities, commonly referred to as radiation effects.[6] Similarly, Fig. 3(d) shows that most acoustic energy dissipation occurs near the walls of the perforation and the Helmholtz neck. Energy dissipation is also significant at the entrance and exit edges of the perforation and the Helmholtz neck, corresponding closely to the regions of strong velocity shear shown in Fig. 3(c). Compared to a conventional Helmholtz resonator, the inclusion of the perforation in the proposed absorber markedly increases the system's viscous losses. Another point of interest to be seen in Fig. 3(d) is that losses can be also observed on the cavity wall. As the cavity wall losses are usually not modeled in such studies, this justifies the extra effort in doing so in this current study.

In order to broaden the sound absorption bandwidth of the MHA while keeping the total area constant and with the extra objective to further reduce the total thickness, we developed a variation involving three individual MHA units, as illustrated in Fig. 4, termed the Compact MHA (CMHA). As shown in Fig. 4(a), the chambers are sequentially numbered from 1 to 6. Each chamber in this design can have a unique depth, denoted as $D(i)$, where i is the chamber number. The number of perforations and their diameter for each MPP are allowed to vary. These dimensions are denoted as $n(i)$ and $d(i)$, respectively. The internal diameter and length of each Helmholtz resonator's neck in this study are also variable. These dimensions are denoted as $d_n(i)$ and $L_n(i)$, respectively. The lengths of each chamber are denoted by L_1–L_6. The width of each chamber is identical, denoted by W_1. The thickness of the *top* plate in the CMHA is symbolized as τ, whereas the thickness of the *internal* adjacent panels and the wall thickness of the Helmholtz resonator's neck are represented by τ'.

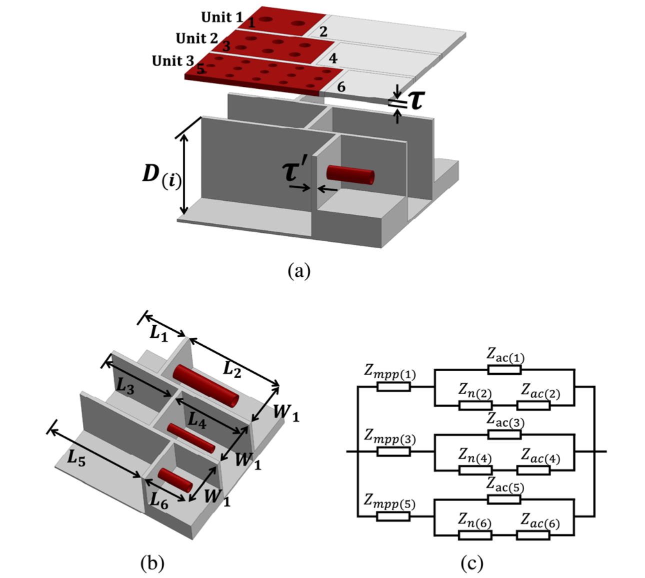

FIG. 4. CMHA design. (a) Structural arrangement of the CMHA. (b) Helmholtz resonators of the CMHA with varying sub-chamber depths (top plane not shown for clarity). (c) Equivalent circuit model of the CMHA.

The total thickness, H, of the CMHA is obtained by summing τ and the maximum sub-chamber depth, D_{max}. The total specific impedance of the CMHA can be derived from the equivalent circuit model, depicted in Fig. 4(c).

In this study, we design and fabricate three CMHAs, designated as CMHA-I, CMHA-II, and CMHA-III. CMHA-I is optimized to achieve broadband sound absorption within the range of [200–500] Hz, CMHA-II within [500–1000] Hz, and CMHA-III within [200–1000] Hz. The broadband optimization process and the optimized geometric parameters of the CMHA samples are detailed in the supplementary material. The CMHA samples are manufactured once again using MSLA. Figure 5(a) shows a photograph of the fabricated CMHA-II. The theoretical and experimental sound absorption curves for CMHA-I, CMHA-II, and CMHA-III are shown in Figs. 5(b)–5(d), demonstrating generally excellent agreement. However, some discrepancies exist between the theoretical and experimental results, particularly for CMHA-I below 250 Hz and CMHA-III below 300 Hz. The primary factors contributing to these discrepancies include (1) potential sealing issues between the sample and the impedance tube, and (2) uncertainties in the manufacturing process. The theoretical absorption curves of individual units in the CMHA are also presented in order to provide some insight into the benefit of the coupling effect. When these units are integrated, the relative absorption bandwidth is significantly broadened in all three CMHA cases due to coupling mechanisms between the units. Moreover, integration results in a reduction in the magnitude of the low-frequency absorption peaks, while the high-frequency absorption peaks tend to increase compared to the magnitude of the individual unit responses. Effective tunable sound absorption can be achieved by varying the geometric parameters of the CMHA. Experimental results demonstrate that CMHA-I, with an overall thickness of 27.5 mm, achieves an average SAC exceeding 0.74 in the frequency range of 300–500 Hz. Similarly, CMHA-II, with a thickness of 26.2 mm, achieves an average SAC exceeding 0.88 in the range of 543–945 Hz. CMHA-III, with an overall thickness of 26.0 mm, achieves an average SAC exceeding 0.84 in the range of 467–912 Hz.

Figure 5(e) compares the sound absorption bandwidth (SAC > 0.6) of CMHA samples with other typical low-frequency, broadband MPP and Helmholtz resonator acoustic metamaterials reported in the literature. The evaluation of acoustic performance is based on the target frequency range, low-frequency sound absorption coefficients, and overall structural thickness. In Fig. 5(e), the red bars represent the data for the CMHA samples, extracted from Figs. 5(b) to 5(d). The yellow bar corresponds to a hybrid sound absorber composed of a micro-perforated panel (MPP) and coiled-up Fabry–Pérot channels, as investigated by Wu *et al.*[21] The magenta bars indicate two acoustic absorbers consisting of a perforated panel with parallel-arranged extended tubes, either with or without an MPP, as described by Li *et al.*[15] The green bar denotes an acoustic absorber integrating Helmholtz resonators with embedded necks and micro-perforations in parallel, as studied by Ryoo *et al.*[24] The dark bar represents a compact acoustic absorber employing a Helmholtz resonator with an embedded spiral neck, as reported by Guo *et al.*[6] The cyan bar corresponds to a single-layer absorber comprising four parallel-arranged inhomogeneous micro-perforated panels, examined by Rafique *et al.*[18] The orange bar signifies a double-layer absorber consisting of multiple parallel-arranged inhomogeneous micro-perforated panels, as explored by Rafique *et al.*[17] The violet bar corresponds to a sound absorber based on MPP and impedance matching coiled-up cavity, examined by Rafique *et al.*[18] The violet bar represents a sound absorber formed by the parallel connection of different units based on an MPP and an impedance-matching coiled-up cavity, as examined by WebPlotDigitizer.[23] In Fig. 5(e), the blue asterisks represent the corresponding total thickness of the absorber. Notably, all compared data are experimental and were extracted directly from the cited literature using WebPlotDigitizer.[43] The CMHA samples exhibit favorable acoustic performance in terms of bandwidth, low-frequency absorption, and overall thickness compared to the referenced designs.

This study investigates the design and evaluation of a low-frequency, broadband, noise-absorbing acoustic metasurface. A basic unit of the metasurface consists of a micro-perforated panel and an extended-neck Helmholtz resonator, referred to as MHA. Experimental results show that near-perfect sound absorption of over 97% can be achieved at 150 Hz with a thickness of 48 mm (sub-wavelength ratio = 1/48). To further broaden the sound absorption bandwidth of the MHA while keeping the total area constant and reducing the total thickness, we propose a variation involving three coupled MHA units, referred to as CMHA. The experimental results demonstrate that the CMHA achieves an average SAC exceeding 0.74 within the 300–500 Hz frequency range, with an overall thickness of only 27.5 mm. Furthermore, the CMHA design achieves an average SAC exceeding 0.88 within the 543–945 Hz range with a reduced thickness of 26.2 mm, and an average SAC exceeding 0.83 within the 467–912 Hz range with a further reduced thickness of 26 mm. The findings make both MHA and CMHA particularly suitable for practical applications where space limitations and low-frequency noise control are crucial.

See the supplementary material for detailed information on (1) the experimental setup; (2) the optimization process; (3) optimized

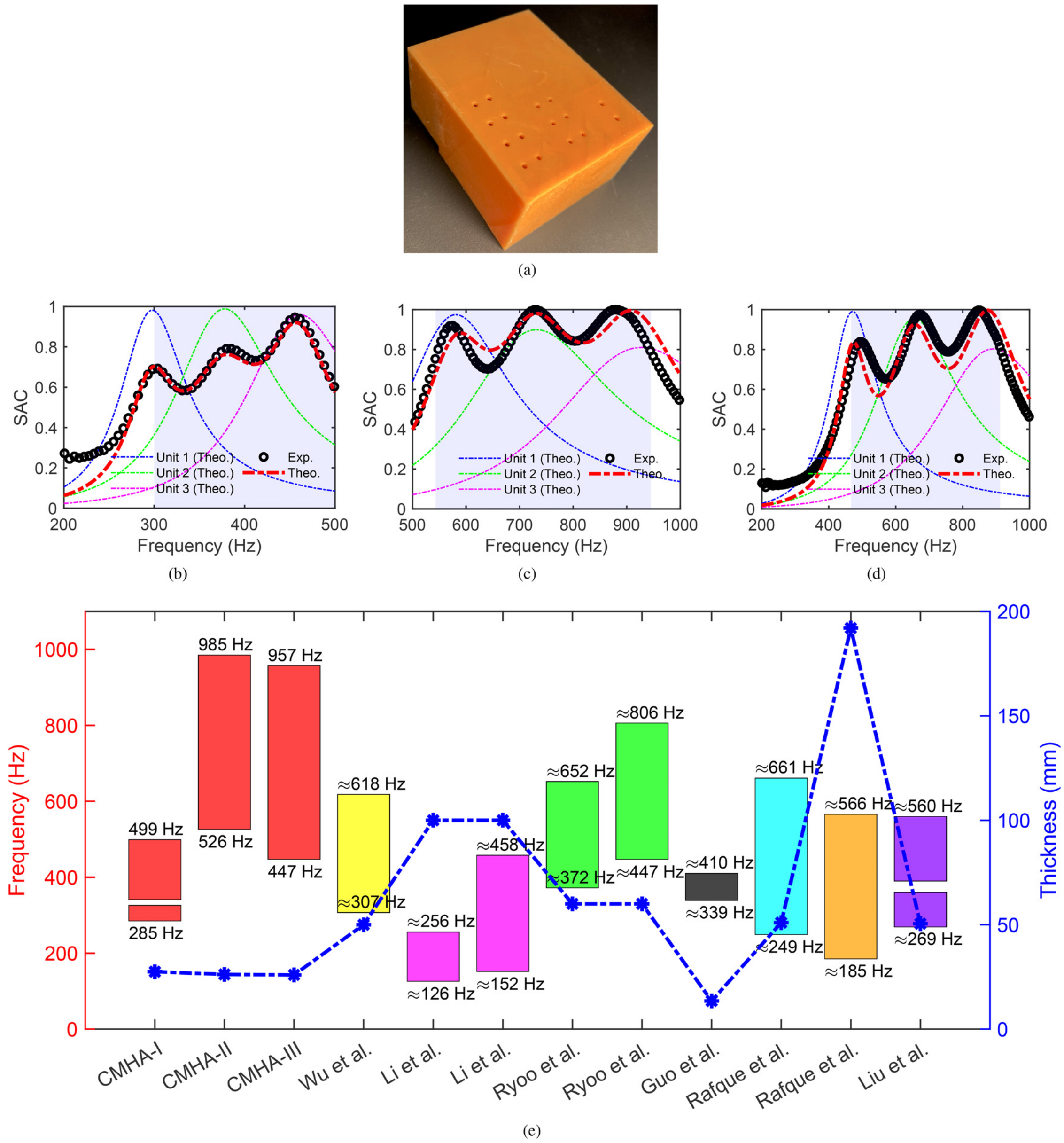

FIG. 5. (a) Photograph of CMHA-II. (b)–(d) The theoretical and experimental SACs of CMHA-I (thickness: 27.5 mm) in the 200–500 Hz range, CMHA-II (thickness: 26.2 mm) in the 500–1000 Hz range, and CMHA-III (thickness: 26.0 mm) in the 200–1000 Hz range. (e) Comparison with the literature of experimental results.

mesh settings; (4) optimized geometric parameters of the MHA and CMHA test samples; (5) relative error analysis; and (6) the effect of the extended neck position on the acoustic performance of the MHA.

This project was funded by the European Union's Horizon 2020 research and innovation program under Grant Agreement No. 860538 for the INVENTOR project. Jiayu Wang received financial support through the China Scholarship Council (CSC)—Trinity College Dublin Joint Scholarship Programme.

AUTHOR DECLARATIONS

Conflict of Interest

The authors have no conflicts to disclose.

Author Contributions

Jiayu Wang: Conceptualization (equal); Data curation (lead); Investigation (lead); Methodology (equal); Software (equal); Visualization (lead); Writing – original draft (equal). **Gareth J. Bennett:** Conceptualization (equal);

Funding acquisition (lead); Methodology (equal); Resources (lead); Software (equal); Supervision (lead); Writing – original draft (lead).

DATA AVAILABILITY

The data that support the findings of this study are available from the corresponding authors upon reasonable request.

REFERENCES

[1] J. Mei, G. Ma, M. Yang, Z. Yang, W. Wen, and P. Sheng, "Dark acoustic metamaterials as super absorbers for low-frequency sound," Nat. Commun. **3**, 756 (2012).

[2] X. Cai, Q. Guo, G. Hu, and J. Yang, "Ultrathin low-frequency sound absorbing panels based on coplanar spiral tubes or coplanar Helmholtz resonators," Appl. Phys. Lett. **105**, 121901 (2014).

[3] K. Mahesh, S. K. Ranjith, and R. S. Mini, "Recent advancements in Helmholtz resonator based low-frequency acoustic absorbers: A critical review," Arch. Comput. Methods Eng. **31**, 2079–2107 (2024).

[4] S. Huang, X. Fang, X. Wang, B. Assouar, Q. Cheng, and Y. Li, "Acoustic perfect absorbers via Helmholtz resonators with embedded apertures," J. Acoust. Soc. Am. **145**, 254–262 (2019).

[5] J. Rayleigh and R. Lindsay, *The Theory of Sound*, 2nd ed. (Dover, New York, 1945).

[6] J. Guo, X. Zhang, Y. Fang, and Z. Jiang, "A compact low-frequency sound-absorbing metasurface constructed by resonator with embedded spiral neck," Appl. Phys. Lett. **117**, 221902 (2020).

[7] W. Zhang and F. Xin, "Broadband low-frequency sound absorption via Helmholtz resonators with porous material lining," J. Sound Vib. **578**, 118330 (2024).

[8] T. Bravo and C. Maury, "Causally-guided acoustic optimization of single-layer rigidly-backed micro-perforated partitions: Theory," J. Sound Vib. **520**, 116634 (2022).

[9] T. Bravo and C. Maury, "Causally-guided acoustic optimization of rigidly-backed micro-perforated partitions: Case studies and experiments," J. Sound Vib. **523**, 116735 (2022).

[10] J. Wang and G. J. Bennett, "Multi-chamber micro-perforated panel absorbers optimised for high amplitude broadband absorption using a two-point impedance method," J. Sound Vib. **547**, 117527 (2023).

[11] J. Wang and G. J. Bennett, "Ultra-broadband sound absorption in a compact multi-chamber micro-perforated panel absorber with varying depths," AIP Adv. **14**, 015009 (2024).

[12] K. Sakagami, M. Morimoto, and W. Koike, "A numerical study of double-leaf microperforated panel absorbers," Appl. Acoust. **67**, 609–619 (2006).

[13] C. Wang and L. Huang, "On the acoustic properties of parallel arrangement of multiple micro-perforated panel absorbers with different cavity depths," J. Acoust. Soc. Am. **130**, 208–218 (2011).

[14] Y. K. Chiang and Y. S. Choy, "Acoustic behaviors of the microperforated panel absorber array in nonlinear regime under moderate acoustic pressure excitation," J. Acoust. Soc. Am. **143**, 538–549 (2018).

[15] D. Li, D. Chang, and B. Liu, "Enhancing the low frequency sound absorption of a perforated panel by parallel-arranged extended tubes," Appl. Acoust. **102**, 126–132 (2016).

[16] W. Yang, Y. Choy, and Y. Li, "Acoustical performance of a wavy micro-perforated panel absorber," Mech. Syst. Signal Proc. **185**, 109766 (2023).

[17] F. Rafique, J. H. Wu, M. Waqas, X. Lushuai, and F. Ma, "A thin double-layer multiple parallel-arranged inhomogeneous microperforated panel absorber for wideband low-frequency sound absorption," J. Braz. Soc. Mech. Sci. Eng. **44**, 31 (2022).

[18] F. Rafique, J. H. Wu, S. M. A. Naqvi, and F. Ma, "Enhanced wideband low-frequency sound absorption of a single-layer multiple parallel-arranged inhomogeneous microperforated panel absorber," Acoust. Aust. **50**, 49–69 (2022).

[19] C. Wang and X. Liu, "Investigation of the acoustic properties of corrugated micro-perforated panel backed by a rigid wall," Mech. Syst. Signal Process. **140**, 106699 (2020).

[20] C. Yang and L. Cheng, "Sound absorption of microperforated panels inside compact acoustic enclosures," J. Sound Vib. **360**, 140–155 (2016).

[21] F. Wu, Y. Xiao, D. Yu, H. Zhao, Y. Wang, and J. Wen, "Low-frequency sound absorption of hybrid absorber based on micro-perforated panel and coiled-up channels," Appl. Phys. Lett. **114**, 151901 (2019).

[22] C. Rui Liu, J. Hui Wu, Z. Yang, and F. Ma, "Ultra-broadband acoustic absorption of a thin microperforated panel metamaterial with multi-order resonance," Compos. Struct. **246**, 112366 (2020).

[23] Y. Liu, S. Ren, W. Sun, Y. Lei, H. Wang, and X. Zeng, "Broadband low-frequency sound absorbing metastructures based on impedance matching coiled-up cavity," Appl. Phys. Lett. **119**, 101901 (2021).

[24] H. Ryoo, K. Yong Lee, and W. Jeon, "Broadband sound absorption using hybrid resonators with embedded necks and micro-perforations in parallel," Mech. Syst. Signal Process. **211**, 111205 (2024).

[25] X. Wang, H. Zhao, X. Luo, and Z. Huang, "Membrane-constrained acoustic metamaterials for low frequency sound insulation," Appl. Phys. Lett. **108**, 041905 (2016).

[26] Z. Yang, J. Mei, M. Yang, N. H. Chan, and P. Sheng, "Membrane-type acoustic metamaterial with negative dynamic mass," Phys. Rev. Lett. **101**, 204301 (2008).

[27] Z. Yang, H. M. Dai, N. H. Chan, G. C. Ma, and P. Sheng, "Acoustic metamaterial panels for sound attenuation in the 50-1000 Hz regime," Appl. Phys. Lett. **96**, 041906 (2010).

[28] A. McKay, I. Davis, J. Killeen, and G. J. Bennett, "SeMSA: A compact super absorber optimised for broadband, low-frequency noise attenuation," Sci. Rep. **10**, 17967 (2020).

[29] I. Davis, A. McKay, and G. J. Bennett, "A graph-theory approach to optimisation of an acoustic absorber targeting a specific noise spectrum that approaches the causal optimum minimum depth," J. Sound Vib. **505**, 116135 (2021).

[30] J. Killeen, I. Davis, J. Wang, and G. J. Bennett, "Fan-noise reduction of data centre telecommunications' server racks, with an acoustic metamaterial broadband, low-frequency sound-absorbing liner," Appl. Acoust. **203**, 109229 (2023).

[31] L. Cao, Q. Fu, Y. Si, B. Ding, and J. Yu, "Porous materials for sound absorption," Compos. Commun. **10**, 25–35 (2018).

[32] X. Liu, X. Ma, C. Yu, and F. Xin, "Sound absorption of porous materials perforated with holes having gradually varying radii," Aerosp. Sci. Technol. **120**, 107229 (2022).

[33] J.-P. Groby, C. Lagarrigue, B. Brouard, O. Dazel, V. Tournat, and B. Nennig, "Using simple shape three-dimensional rigid inclusions to enhance porous layer absorption," J. Acoust. Soc. Am. **136**, 1139–1148 (2014).

[34] D.-Y. Maa, "Potential of microperforated panel absorber," J. Acoust. Soc. Am. **104**, 2861–2866 (1998).

[35] M. A. Temiz, I. Lopez Arteaga, G. Efraimsson, M. Åbom, and A. Hirschberg, "The influence of edge geometry on end-correction coefficients in micro perforated plates," J. Acoust. Soc. Am. **138**, 3668–3677 (2015).

[36] J.-P. Dalmont, C. Nederveen, and N. Joly, "Radiation impedance of tubes with different flanges: Numerical and experimental investigations," J. Sound Vib. **244**, 505–534 (2001).

[37] W. Kampinga, "Viscothermal acoustics using finite elements—Analysis tools for engineers," Ph.D. thesis (University of Twente, Netherlands, 2010).

[38] J. Carbajo, J. Ramis, L. Godinho, and P. Amado-Mendes, "Perforated panel absorbers with micro-perforated partitions," Appl. Acoust. **149**, 108–113 (2019).

[39] ISO, "Acoustics—Determination of sound absorption coefficient and impedance in impedance tubes—Part 2: Transfer-function method," International Standard 10534-2:2023 (ISO, 2023).

[40] V. Romero-García, G. Theocharis, O. Richoux, and V. Pagneux, "Use of complex frequency plane to design broadband and sub-wavelength absorbers," J. Acoust. Soc. Am. **139**, 3395–3403 (2016).

[41] V. Romero-García, G. Theocharis, O. Richoux, A. Merkel, V. Tournat, and V. Pagneux, "Perfect and broadband acoustic absorption by critically coupled sub-wavelength resonators," Sci. Rep. **6**, 19519 (2016).

[42] V. Hruška, J.-P. Groby, and M. Bednařík, "Complex frequency analysis and source of losses in rectangular sonic black holes," J. Sound Vib. **571**, 118107 (2024).

[43] A. Rohatgi, see https://automeris.io for "WebPlotDigitizer (v5.2)" (2024).